

6. We used the same observed data as IPCC, updated (P. D. Jones, personal communication). For sources, see: N. Nicholls *et al.*, in *Climate Change 1995: The Science of Climate Change*, J. T. Houghton *et al.*, Eds. (Cambridge Univ. Press, Cambridge, 1996), pp. 133–192. Our analyses span 1881–1996. The conclusions of this paper do not depend on the precise start or end points.
7. We use data from two 1000-year unforced simulations with coupled ocean/atmosphere general circulation models: the Geophysical Fluid Dynamics Laboratory (GFDL) model [S. Manabe and R. J. Stouffer, *J. Clim.* **9**, 376 (1996)]; and the U.K. Hadley Centre model (HadCM2) [S. F. B. Tett, T. C. Johns, J. F. B. Mitchell, *Clim. Dyn.* **13**, 303 (1997)]. For the control-run results we used the full areal coverage to define the hemispheric means. For the observed data, coverage is incomplete and tends to increase with time. To test whether such coverage differences affected our results, we masked the control-run data with typical observed coverages and re-computed the correlations. The results were similar to the full-coverage results. Standard errors associated with the sample autocorrelations are typically of the order 0.05 or smaller in the case of the model data, and in the range 0.1 to 0.15 for the observational data. These were calculated by applying standard asymptotic formulae for the variance of sample autocorrelations [for example, see p. 342 of W. A. Fuller, *Introduction to Statistical Time Series*, (Wiley-Interscience, ed. 2, New York, 1996)]. In doing so, we assume that the true autocorrelations used for calculating the theoretical results are those estimated from the model data. The result that the standard errors are larger for the observed series than the model series reflects the difference in sample sizes (116 against 1000). These results were also checked from the model data using a resampling procedure, based on the empirical standard deviation of sample autocorrelations calculated from maximally overlapping 116-year subseries of the 1000-year model runs; this produced results consistent with the asymptotic formulae. The results show that the difference between sample autocorrelations for the observed and either of the control-run series are 2 to 3 times the standard errors for the observed series. On this basis we conclude that the two sets of autocorrelations are indeed significantly different.
8. From HadCM2 [T. C. Johns *et al.*, *Clim. Dyn.* **13**, 103 (1997); J. F. B. Mitchell and T. C. Johns, *J. Clim.* **10**, 245 (1997)]. In these simulations, which span the period 1861–2100, greenhouse-gas effects were modeled using observed CO₂ changes inflated to account for non-CO₂ greenhouse gases, and sulfate aerosol effects were modeled by using changes in surface albedo.
9. T. M. L. Wigley and S. C. B. Raper, *Nature* **357**, 293 (1992); S. C. B. Raper, T. M. L. Wigley, R. A. Warrick, in *Sea-Level Rise and Coastal Subsidence: Causes, Consequences and Strategies*, J. D. Milliman and B. U. Haq, Eds. (Kluwer, Dordrecht, Netherlands, 1996), pp. 11–45. Simulations run from 1765 through 1996. The model differentiates between land and ocean in each hemisphere and gives hemispherically-specific temperature change results.
10. P. D. Jones, *Clim. Mon.* **17**, 80 (1988); updated (P. D. Jones, personal communication).
11. Reviewed by C. K. Folland, T. R. Karl, K. Ya. Vinnikov, in *Climate Change. The IPCC Scientific Assessment*, J. T. Houghton, G. J. Jenkins, J. J. Ephraums, Eds. (Cambridge Univ. Press, Cambridge, 1990), pp. 195–238; C. K. Folland *et al.*, in *Climate Change 1992: The Supplementary Report to the IPCC Scientific Assessment*, J. T. Houghton, B. A. Callander, S. K. Varney, Eds. (Cambridge Univ. Press, Cambridge, 1992), pp. 135–170; and by N. Nicholls *et al.* (6).
12. A. Kattenberg *et al.*, in *Climate Change 1995: The Science of Climate Change*, J. T. Houghton *et al.*, Eds. (Cambridge Univ. Press, Cambridge, 1996), pp. 285–357.
13. We have, nevertheless, tested this by subtracting estimated volcanic effects for all known major eruptions from the observed data. The influence on the autocorrelation structure is negligible.
14. D. V. Hoyt and K. H. Schatten, *J. Geophys. Res.* **98**, 18895 (1994). Other reconstructions, such as by J. L. Lean, J. Beer, and R. Bradley [*Geophys. Res. Lett.* **22**, 3195 (1995)], are similar. The results presented here do not depend on which solar data set is used.
15. The forcings used in the U-D model are the estimates employed by IPCC (12). Greenhouse gases included are CO₂, CH₄, N₂O, tropospheric and stratospheric ozone, and halocarbons. Aerosols included are the direct and indirect effects of sulfates and aerosols from biomass burning. Extensions beyond 1990 were made using the IS92a emissions scenario and observed CO₂ data. The IS92a scenario is the central “existing policies” scenario produced by IPCC in 1992 [J. A. Leggett, W. J. Pepper, R. J. Swart, in *Climate Change 1992: The Supplementary Report to the IPCC Scientific Assessment*, J. T. Houghton, B. A. Callander, S. K. Varney, Eds. (Cambridge Univ. Press, Cambridge, 1992), pp. 69–95]. The modifications made to this scenario are described in T. M. L. Wigley, *Geophys. Res. Lett.* **25**, 2285 (1998).
16. The climate sensitivity (that is, the sensitivity to external forcing) is the equilibrium global-mean warming per unit radiative forcing, commonly expressed as the global-mean warming for a doubling of the CO₂ concentration, ΔT_{2x} . The most likely range for ΔT_{2x} is 1.5–4.5°C [J. F. B. Mitchell *et al.*, in *Climate Change. The IPCC Scientific Assessment*, J. T. Houghton, G. J. Jenkins, J. J. Ephraums, Eds. (Cambridge Univ. Press, Cambridge, 1990), pp. 131–172] representing roughly the 90% confidence interval. The concept may be applied to any forcing. For example, the equilibrium global-mean warming for a 1% increase in solar irradiance (2.4 W/m²) would be 2.4($\Delta T_{2x}/\Delta Q_{2x}$) where ΔQ_{2x} is the forcing for 2x CO₂ (approx. 4 W/m²).
17. T. M. L. Wigley, P. D. Jones, S. C. B. Raper, *Proc. Natl. Acad. Sci. U.S.A.* **94**, 8314 (1997). Note that these climate sensitivities depend on the assumed magnitudes of anthropogenic and solar forcing. In particular, they vary considerably if the magnitude of aerosol forcing is altered within the (large) uncertainty range of this component.
18. These values differ slightly from those in (17) because we use a different optimization interval.
19. We do this by fitting the U-D model (8) results for anthropogenic-plus-solar forcing to the observations (best-fit sensitivity 3.2°C) and then disaggregating the hemispheric-mean modeled temperatures into their solar, effective sulfate aerosol (see below), and residual anthropogenic components. The “effective aerosol” response is the sum of responses to direct and indirect sulfate aerosol forcing and tropospheric ozone. HadCM2 considers only direct sulfate aerosol forcing. Because its magnitude and pattern are similar to the effective aerosol forcing used in the U-D model, we considered the two to be equivalent for the purposes of producing adjusted-observed data.
20. Solar-plus-aerosol forcing leads to cooling. Thus, removing this component gives residuals with a larger positive trend than in the raw data.
21. G. A. Meehl, G. J. Boer, C. Covey, M. Latif, R. J. Stouffer, *Eos* **78**, 445 (1997).
22. Supported by USDOE (T.M.L.W. and B.D.S.), NOAA (Award No. NA87GP0105 to T.M.L.W.) and NSF (DMS-9705166 to R.L.S.). Observed temperatures from P.D. Jones and D.E. Parker; control-run GCM data provided through the CMIP (21) project; SUL and GHG data provided by J.M. Gregory. NCAR is sponsored by the National Science Foundation.

16 September 1998; accepted 2 November 1998

A Dielectric Omnidirectional Reflector

Yoel Fink, Joshua N. Winn, Shanhui Fan, Chiping Chen, Jurgen Michel, John D. Joannopoulos, Edwin L. Thomas*

A design criterion that permits truly omnidirectional reflectivity for all polarizations of incident light over a wide selectable range of frequencies was used in fabricating an all-dielectric omnidirectional reflector consisting of multilayer films. The reflector was simply constructed as a stack of nine alternating micrometer-thick layers of polystyrene and tellurium and demonstrates omnidirectional reflection over the wavelength range from 10 to 15 micrometers. Because the omnidirectionality criterion is general, it can be used to design omnidirectional reflectors in many frequency ranges of interest. Potential uses depend on the geometry of the system. For example, coating of an enclosure will result in an optical cavity. A hollow tube will produce a low-loss, broadband waveguide, whereas a planar film could be used as an efficient radiative heat barrier or collector in thermoelectric devices.

Mirrors, probably the most prevalent of optical devices, are used for imaging and solar energy collection and in laser cavities. One can distinguish between two types of

mirrors, the age-old metallic and the more recent dielectric. Metallic mirrors reflect light over a broad range of frequencies incident from arbitrary angles (that is, omnidirectional reflectance). However, at infrared and optical frequencies, a few percent of the incident power is typically lost because of absorption. Multilayer dielectric mirrors are used primarily to reflect a narrow range of frequencies incident from a particular angle or particular angular range. Unlike their metallic counterparts, dielectric reflectors can be extremely low loss. The ability to reflect light of arbitrary angle of incidence for all-dielectric structures has been associated with the existence of a

Y. Fink, Department of Material Science and Engineering and Plasma Science and Fusion Center, Massachusetts Institute of Technology, Cambridge, MA 02139, USA. J. N. Winn, S. Fan, J. D. Joannopoulos, Department of Physics, Massachusetts Institute of Technology, Cambridge, MA 02139, USA. C. Chen, Plasma Science and Fusion Center, Massachusetts Institute of Technology, Cambridge, MA 02139, USA. J. Michel and E. L. Thomas, Department of Material Science and Engineering, Massachusetts Institute of Technology, Cambridge, MA 02139, USA.

*To whom correspondence should be addressed.

complete photonic band gap (1–3), which can exist only in a system with a dielectric function that is periodic along three orthogonal directions. In fact, a recent theoretical analysis predicted that a sufficient condition for the achievement of omnidirectional reflection in a periodic system with an interface is the existence of an overlapping

band gap regime in phase space above the light cone of the ambient media (4). Now we extend the theoretical analysis and provide experimental realization of a multilayer omnidirectional reflector operable in infrared frequencies. The structure is made of thin layers of materials with different dielectric constants (polystyrene and tellu-

rium) and combines characteristic features of both the metallic and dielectric mirrors. It offers metallic-like omnidirectional reflectivity together with frequency selectivity and low-loss behavior typical of multilayer dielectrics.

We consider a system that is made of an array of alternating dielectric layers coupled to a homogeneous medium, characterized by n_0 (such as air with $n_0 = 1$), at the interface. Electromagnetic waves are incident upon the multilayer film from the homogeneous medium. Although such a system has been analyzed extensively in the literature (5–7), the possibility of omnidirectional reflectivity was not recognized until recently. The generic system is described by the index of refraction profile in Fig. 1, where h_1 and h_2 are the layer thickness and n_1 and n_2 are the indices of refraction of the respective layers. The incident wave has a wave vector $\mathbf{k} = k_x \hat{e}_x + k_y \hat{e}_y$, and a frequency of $\omega = c|k|/n_0$, where c is the speed of light in vacuum and \hat{e}_x and \hat{e}_y are unit vectors in the x and y directions, respectively. The wave vector together with the normal to the periodic structure defines a mirror plane of symmetry that allows us to distinguish between two independent electromagnetic modes: transverse electric (TE) modes and transverse magnetic (TM) modes. For the TE mode, the electric field is perpendicular to the plane, as is the magnetic field for the TM mode. The distribution of the electric field of the TE mode (or the magnetic field in the TM mode) in a particular layer within the stratified structure can be written as a sum of two plane waves traveling in opposite directions. The amplitudes of the two plane waves in a particular layer α of one cell are related to the amplitudes in the same layer of an adjacent cell by a unitary 2×2 translation matrix $U^{(\alpha)}$ (7).

General features of the transport properties of the finite structure can be understood when the properties of the infinite structure are elucidated. In a structure with an infinite number of layers, translational symmetry along the direction perpendicular to the layers leads to Bloch wave solutions of the form

$$E_K(x, y) = E_K(x) e^{iKx} e^{ik_y y} \quad (1)$$

where $E_K(x, y)$ is a field component, $E_K(x)$ is periodic, with a period of length a , and K is the Bloch wave number given by

$$K = \frac{i}{a} \ln \left(\frac{1}{2} \text{Tr}(U^{(\alpha)}) \pm \left\{ \frac{1}{4} [\text{Tr}(U^{(\alpha)})]^2 - 1 \right\}^{1/2} \right) \quad (2)$$

Solutions of the infinite system can be propagating or evanescent, corresponding

Fig. 1. Schematic of the multilayer system showing the layer parameters (n_α and h_α are the index of refraction and thickness of layer α , respectively), the incident wave vector \mathbf{k} , and the electromagnetic mode convention. E and B are the electric and magnetic fields, respectively.

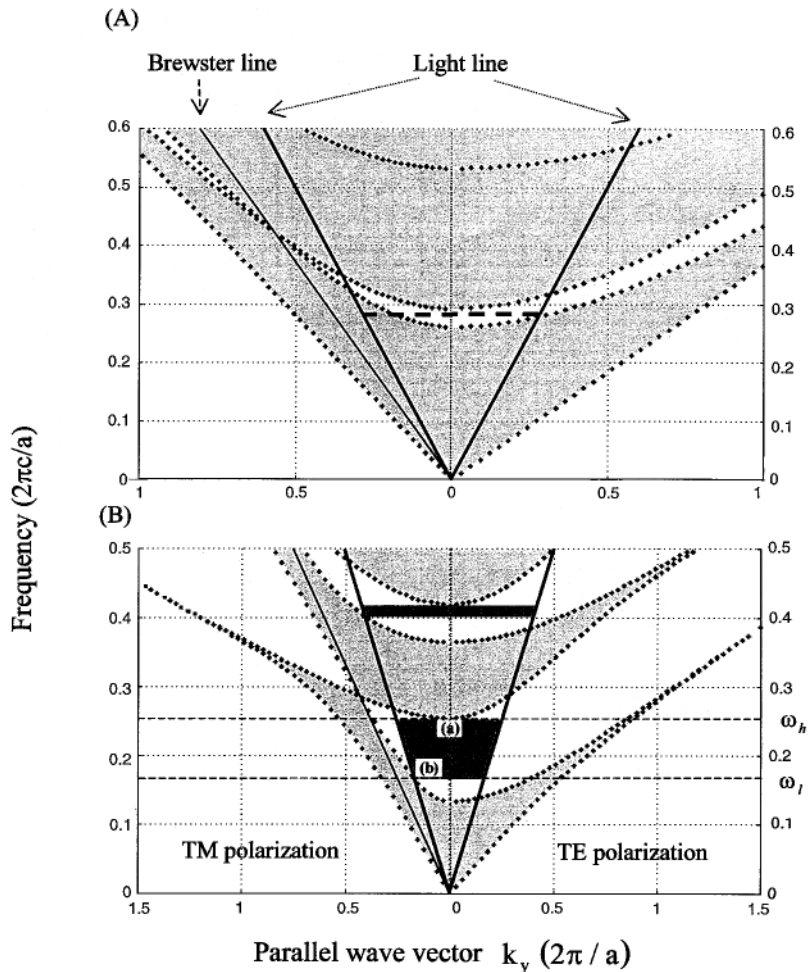
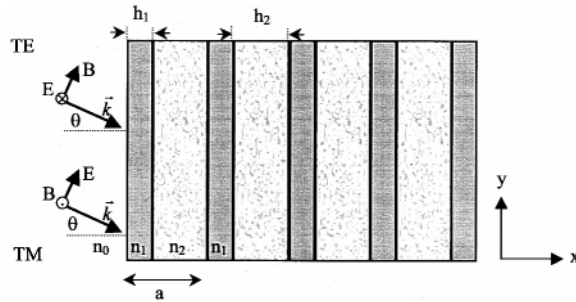


Fig. 2. (A) Projected band structure of a multilayer film with the light line and Brewster line, exhibiting a reflectivity range of limited angular acceptance with $n_0 = 1$, $n_1 = 2.2$ and $n_2 = 1.7$ and a thickness ratio of $h_2/h_1 = 2.2/1.7$. (B) Projected band structure of a multilayer film together with the light line and Brewster line, showing an omnidirectional reflectance range at the first and second harmonic. Propagating states, light gray; evanescent states, white; and omnidirectional reflectance range, dark gray. The film parameters are $n_1 = 4.6$ and $n_2 = 1.6$ with a thickness ratio of $h_2/h_1 = 1.6/0.8$. These parameters are similar to the actual polystyrene-tellurium film parameters measured in the experiment.

to real or imaginary Bloch wave numbers, respectively. The solution of Eq. 2 defines the band structure for the infinite system, $\omega(K, k_y)$. It is convenient to display the solutions of the infinite structure by projecting the $\omega(K, k_y)$ function onto the ω - k_y plane; Examples of such projected structures are shown in Fig. 2, A and B. The light gray areas highlight phase space where K is strictly real, that is, regions of propagating states, whereas the white areas represent regions containing evanescent states. The shape of the projected band structures for the multilayer film can be understood intuitively. At $k_y = 0$, the band gap for waves traveling normal to the layers is recovered. For $k_y > 0$, the bands curve upward in frequency. As $k_y \rightarrow \infty$, the modes become largely confined to the slabs with the high index of refraction and do not couple between layers (and are therefore independent of k_x).

For a finite structure, the translational symmetry in the directions parallel to the layers is preserved; hence, k_y remains a conserved quantity. In the direction perpendicular to the layers, the translational symmetry no longer exists. Nevertheless, the K number, as defined in Eq. 2, is still relevant, because it is determined purely by the dielectric and structural property of a single bilayer. In regions where K is imaginary, the electromagnetic field is strongly attenuated. As the number of layers is increased, the transmission coefficient decreases exponentially, whereas the reflectivity approaches unity.

Because we are primarily interested in waves originating from the homogeneous medium external to the periodic structure, we will focus only on the portion of phase space lying above the light line. Waves originating from the homogeneous medium satisfy the condition $\omega \geq ck_y/n_0$, where n_0 is the refractive index of the homogeneous medium, and therefore they must reside above the light line. States of the homogeneous medium with $k_y = 0$ are normal incident, and those lying on the $\omega = ck_y/n_0$ line with $k_x = 0$ are incident at an angle of 90° .

The states in Fig. 2A that are lying in the restricted phase space defined by the light line and that have a (ω, k_y) corresponding to the propagating solutions (gray areas) of the crystal can propagate in both the homogeneous medium and the structure. These waves will partially or entirely transmit through the film. Those states with (ω, k_y) in the evanescent regions (white areas) can propagate in the homogeneous medium but will decay in the crystal—waves corresponding to this portion of phase space will be reflected off the structure.

The multilayer system leading to Fig. 2A represents a structure with a limited reflectivity cone because for any frequency one can always find a k_y vector for which a wave at that frequency can propagate in the crystal and hence transmit through the film. For example, a wave with $\omega = 0.285 \times 2\pi c/a$ (dashed horizontal line in Fig. 2A) will be reflected for a range of k_y values ranging from 0 (normal incidence) to $0.285 \times 2\pi/a$ (90° incidence) in the TE mode, whereas in the TM mode it begins to transmit at a value of $k_y = 0.187 \times 2\pi/a$ ($\sim 41^\circ$ incidence). The necessary and sufficient criterion (8) for omnidirectional reflectivity at a given frequency is that no transmitting state of the structure exists inside the light cone; this criterion is satisfied by frequency ranges marked in dark gray in Fig. 2B. In fact, the system leading to Fig. 2B exhibits two omnidirectional reflectivity ranges.

The omnidirectional range is defined from above by the normal incidence band edge $\omega_h(k_x = \pi/a, k_y = 0)$ (point a in Fig. 2B) and from below by the intersection of the top of the TM allowed band edge with the light line $\omega_l(k_x = \pi/a, k_y = \omega_l/c)$ (point b in Fig. 2B).

The exact expression for the band edges is

$$\frac{1 + \Lambda}{2} \cos(k_x^{(1)}h_1 + k_x^{(2)}h_2) + \frac{1 - \Lambda}{2} \cos(k_x^{(1)}h_1 - k_x^{(2)}h_2) + 1 = 0, \quad (3)$$

where $k_x^{(\alpha)} = \sqrt{(\omega n_\alpha/c)^2 - k_y^2}$ ($\alpha = 1, 2$) and

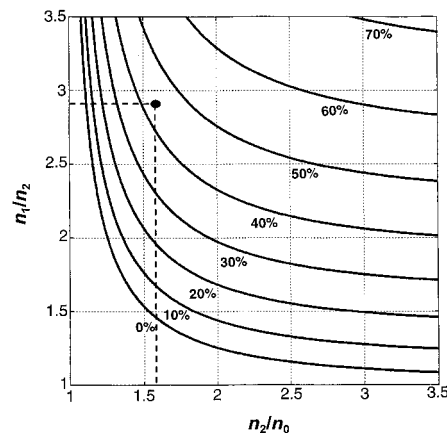


Fig. 3. (left). The range to midrange ratio $(\omega_h - \omega_l)/1/2(\omega_h + \omega_l)$, for the fundamental frequency range of omnidirectional reflection, plotted as contours. Here, the layers were set to quarter wave thickness and $n_1 > n_2$. The ratio for our materials is about 45% ($n_1/n_2 = 2.875$ and $n_2/n_0 = 1.6$). It is located at the intersection of the dashed lines (black dot).

$$\Lambda \equiv \begin{cases} \frac{1}{2} \left(\frac{k_x^{(2)}}{k_x^{(1)}} + \frac{k_x^{(1)}}{k_x^{(2)}} \right) \text{ TE} \\ \frac{1}{2} \left(\frac{n_1^2 k_x^{(2)}}{n_2^2 k_x^{(1)}} + \frac{n_2^2 k_x^{(1)}}{n_1^2 k_x^{(2)}} \right) \text{ TM} \end{cases} \quad (4)$$

A dimensionless parameter used to quantify the extent of the omnidirectional range is the range to midrange ratio defined as $(\omega_h - \omega_l)/1/2(\omega_h + \omega_l)$. Figure 3 is a plot of this ratio as a function of n_2/n_1 and n_1/n_0 , where ω_h and ω_l are determined by solutions of Eq. 3 with quarter wave layer thickness. The contours in this figure represent various equiomnidirectional ranges for different material index parameters and could be useful for design purposes.

It may also be useful to have an approximate analytical expression for the extent of the gap. This can be obtained by setting $\cos(k_x^{(1)}h_1 - k_x^{(2)}h_2) \cong 1$ in Eq. 3. We find that for a given incident angle θ_0 , the approximate width in frequency is

$$\Delta\omega(\theta_0) = \frac{2c}{h_1 \sqrt{n_1^2 - n_0^2 \sin^2 \theta_0} + h_2 \sqrt{n_2^2 - n_0^2 \sin^2 \theta_0}} \times \left[\cos^{-1} \left(-\sqrt{\frac{\Lambda - 1}{\Lambda + 1}} \right) - \cos^{-1} \left(\sqrt{\frac{\Lambda - 1}{\Lambda + 1}} \right) \right] \quad (5)$$

At normal incidence, there is no distinction between TM and TE modes. At increasingly oblique angles, the gap of the TE mode increases, whereas the gap of the TM mode decreases. In addition, the center of the gap shifts to higher frequencies. Therefore, the

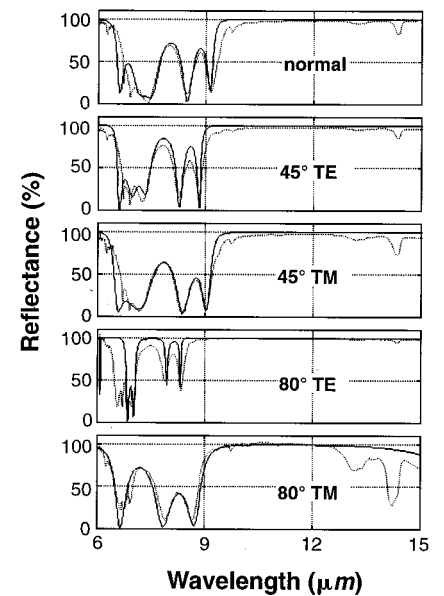


Fig. 4 (right). Calculated (solid line) and measured (dashed line) reflectance (in percent) as a function of wavelength for TM and TE modes at normal, 45° , and 80° angles of incidence, showing an omnidirectional reflectivity band.

criterion for the existence of omnidirectional reflectivity can be restated as the occurrence of a frequency overlap between the gap at normal incidence and the gap of the TM mode at 90°. Analytical expressions for the range to midrange ratio can be obtained by setting

$$\omega_h = \frac{2c}{h_2 n_2 + h_1 n_1} \cos^{-1} \left(- \left| \frac{n_1 - n_2}{n_1 + n_2} \right| \right) \quad (6a)$$

$$\omega_l = \frac{2c}{h_2 \sqrt{n_2^2 - n_0^2} + h_1 \sqrt{n_1^2 - n_0^2}} \times \cos^{-1} \left(\left| \frac{n_1^2 \sqrt{n_2^2 - n_0^2} - n_2^2 \sqrt{n_1^2 - n_0^2}}{n_1^2 \sqrt{n_2^2 - n_0^2} + n_2^2 \sqrt{n_1^2 - n_0^2}} \right| \right) \quad (6b)$$

Moreover, the maximum range width is attained for thickness values that are not equal to the quarter wave stack although the increase in band width gained by deviating from the quarter wave stack is typically only a few percent (4).

In general, the TM mode defines the lower frequency edge of the omnidirectional range. An example can be seen in Fig. 2B for a particular choice of the indices of refraction. This can be proven by showing that

$$\left. \frac{\partial \omega}{\partial k_y} \right|_{\text{TM}} \geq \left. \frac{\partial \omega}{\partial k_y} \right|_{\text{TE}} \quad (7)$$

in the region that resides inside the light line. The physical reason for Eq. 7 lies in the vectorial nature of the electric field. In the upper portion of the first band, the electric field concentrates its energy in the high dielectric regions. Away from normal incidence, the electric field in the TM mode has a component in the direction of periodicity, and this component forces a larger portion of the electric field into the low dielectric regions. The group velocity of the TM mode is therefore enhanced. In contrast, the electric field of the TE mode is always perpendicular to the direction of periodicity and can concentrate its energy primarily in the high dielectric region.

A polystyrene-tellurium (PS-Te) materials system was chosen to demonstrate omnidirectional reflectivity. Tellurium has a high index of refraction and low loss characteristics in the frequency range of interest. In addition, its relatively low latent heat of condensation together with the high glass transi-

tion temperature of the PS minimizes diffusion of Te into the polymer layer. The choice of PS, which has a series of absorption peaks in the measurement range (9), demonstrates the competition between reflectivity and absorption that occurs when an absorption peak is located in the evanescent state region. The Te (0.8 μm) and PS (1.65 μm) films were deposited (10) sequentially to create a nine-layer film (11).

The optical response of this particular multilayer film was designed to have a high reflectivity region in the 10- to 15-μm range for any angle of incidence (in the experiment, we measure from 0° to 80°). The optical response at oblique angles of incidence was measured with a Fourier Transform Infrared Spectrometer (Nicolet 860) fitted with a polarizer (ZnS; SpectraTech) and an angular reflectivity stage (VeeMax; SpectraTech). At normal incidence, the reflectivity was measured with a Nicolet Infrared Microscope. A freshly evaporated aluminum mirror was used as a background for the reflectance measurements.

Good agreement between the calculated (12) and measured reflectance spectra at normal, 45°, and 80° incidence for the TM and TE modes is shown in Fig. 4. The regimes of high reflectivity at the different angles of incidence overlap, thus forming a reflective range of frequencies for light of any angle of incidence. The frequency location of the omnidirectional range is determined by the layer thickness and can be tuned to meet specifications. The range is calculated from Eq. 6 to be 5.6 μm, and the center wavelength is 12.4 μm, corresponding to a 45% range to midrange ratio shown in dashed lines in Fig. 3 for the experimental index of refraction parameters. These values are in agreement with the measured data. The calculations are for lossless media and therefore do not predict the PS absorption band at ~13 and 14 μm. The PS absorption peak is seen to increase at larger angles of incidence for the TM mode and to decrease for the TE mode. The physical basis for these phenomena lies in the relation between the penetration depth and the amount of absorption. The penetration depth is $\xi \propto \text{Im}(1/K)$, where K is the Bloch wave number. It can be shown that ξ is a monotonically increasing function of the incident angle for the TM mode of an omnidirectional reflector and is relatively constant for the TE mode. Thus, the TM mode penetrates deeper into the structure at increasing angles of incidence (Table 1) and is more readily absorbed. The magnitude of the imaginary part of the Bloch wave number for a mode lying in the gap is related to its distance from the band edges. This distance increases in the TE mode because of the widening of the gap at increasing angles of incidence and decreases in the TM mode because of the shrinking of the gap.

The PS-Te structure does not have a complete photonic band gap. Its omnidirectional reflectivity is due instead to the restricted phase space available to the propagating states of the system. The materials and processes were chosen for their low cost and applicability to large area coverage. The possibility of achieving omnidirectional reflectivity itself is not associated with any particular choice of materials and can be applied to many wavelengths of interest. Our structure offers metallic-like omnidirectional reflectivity for a wide range of frequencies and at the same time is of low loss. In addition, it allows the flexibility of frequency selection.

References and Notes

1. E. Yablonovitch, *Phys. Rev. Lett.* **58**, 2059 (1987).
2. S. John, *ibid.*, p. 2486.
3. J. D. Joannopoulos, R. Meade, J. N. Winn, *Photonic Crystals: Molding the Flow of Light* (Princeton Univ. Press, Princeton, NJ, 1995).
4. J. N. Winn *et al.*, *Opt. Lett.*, **23**, 1573 (1998).
5. F. Abeles, *Ann. Phys.* **5**, 706 (1950).
6. M. Born and E. Wolf, *Principles of Optics* (Pergamon, ed. 6, 1980), p. 67.
7. P. Yeh *et al.*, *J. Opt. Soc. Am.* **67**, 423 (1977).
8. A necessary condition for omnidirectional reflectivity is that light from outside the film cannot be allowed to access the Brewster angle $\theta_b = \tan^{-1}(n_1/n_2)$ of the multilayer structure because at this angle the TM mode will be transmitted through. This condition is met when the Brewster line lies outside of the light line or in terms of the refractive indices of the layers $\sin^{-1}(n_0/n_2) < \theta_b$. A sufficient condition is the existence of a particular frequency at which no propagating mode within the crystal exists between $k_y = 0$ and $k_y = n_0 \omega/c$. Figure 2A is an example of a structure that does not have an omnidirectional reflectivity range even though its Brewster crossing is inaccessible to light coming from the homogeneous medium (the Brewster crossing lies outside the light cone). This is due to the large group velocity of modes in the lower band edge of the TM mode that allow every frequency to couple to a propagating state in the crystal. This should be contrasted with Fig. 2B, which exhibits an omnidirectional reflectivity range (highlighted in dark gray); the high indices of refraction actually allow for the opening of an additional omnidirectional reflectivity range in the higher harmonic as well.
9. C. J. Pouchert, *The Aldrich Library of FT-IR Spectra*, vol. II (Aldrich Chemical, Milwaukee, WI, 1985), p. 1204B.
10. A 0.8 ± 0.09-μm-thick layer of tellurium (99.99+%; Strem Chemicals) was vacuum evaporated at 10⁻⁶ torr and 7A (Ladd Industries 30000) onto a NaCl 25-mm salt substrate (polished NaCl window; Wilmad Glass). The layer thickness and deposition rate were monitored in situ with a crystal thickness monitor (Sycon STM100). A 10% solution of polystyrene (Goodyear PS standard, 110,000 g/mol) in toluene was spin cast at 1000 rpm onto the tellurium-coated substrate and allowed to dry for a few hours; the polymer layer thickness is 1.65 ± 0.09 μm.
11. The nine-layer film sequence was Te/PS/Te/PS/Te/PS/Te/PS/Te.
12. The calculations were done with the transfer matrix method described in (5) with the film parameters.
13. We thank J. F. Hester and A. Urbas for their valuable assistance and M. G. Bawendi and G. B. Kenney for stimulating discussions and inspiration. Supported in part by Defense Advanced Research Agency through U.S. Army Research Office under grant DAAG55-97-1-0366 and by the Air Force Office of Scientific Research under grants F49620-97-1-0325 and F49620-97-1-0385.

6 August 1998; accepted 6 October 1998

Table 1. Penetration depth (ξ) at different angles of incidence for the TE and TM modes.

Angle of incidence (degrees)	ξ _{TM} (μm)	ξ _{TE} (μm)
0	2.51	2.51
45	3.05	2.43
80	4.60	2.39